Biogeosciences Discuss., 11, 4949–4993, 2014
www.biogeosciences-discuss.net/11/4949/2014/
doi:10.5194/bgd-11-4949-2014

Biogeosciences Discussions
Open Access

Rapid formation of large aggregates during the spring bloom of Kerguelen Island: observations and model comparisons

M.-P. Jouandet[1], G. A. Jackson[2], F. Carlotti[1], M. Picheral[3], L. Stemmann[4], and S. Blain[5,6]

[1]Mediterranean Institute of Oceanography (MIO), Unité mixte: Aix Marseille Université – CNRS – IRD, 13288 Marseille Cedex 09, France
[2]Department of Oceanography, Texas A&M University, College Station, TX 77845-3146, USA
[3]CNRS, UMR 7093, LOV, Observatoire océanologique, 06230, Villefranche/mer, France
[4]Sorbonne Universités, UPMC Univ Paris 06, UMR 7093, LOV, Observatoire océanologique, 06230, Villefranche/mer, France
[5]Sorbonne Universités, UPMC Univ Paris 06, UMR 7621, Laboratoire d'Océanographie Microbienne, Observatoire Océanologique, 66650 Banyuls/mer, France
[6]CNRS, UMR 7621, Laboratoire d'Océanographie Microbienne, Observatoire Océanologique, 66650 Banyuls/mer, France

Received: 17 March 2014 – Accepted: 18 March 2014 – Published: 28 March 2014

Correspondence to: M.-P. Jouandet (jouandetmariepaule@yahoo.fr) and G. Jackson (gjackson@tamu.edu)

Published by Copernicus Publications on behalf of the European Geosciences Union.

Abstract

We recorded vertical profiles of particle size distributions (PSD, sizes ranging from 0.052 to several mm in equivalent spherical diameter) in the natural iron-fertilized bloom southeast of Kerguelen Island (Southern Ocean) from pre-bloom to early bloom stage. PSD were measured by the Underwater Vision Profiler during the Kerguelen Ocean and Plateau Compared Study cruise 2 (KEOPS 2, October–November 2011). The total particle numerical abundance was more than 4 fold higher during the early bloom phase compared to pre-bloom conditions as a result of the 2-weeks bloom development. We witnessed the rapid formation of large particles and their accumulation at the base of the mixed layer within a two days period, as indicated by changes in total particle volume (V_T) and particle size distribution. The V_T profiles suggest sinking of particles from the mixed layer to 200 m, but little export deeper than 200 m during the observation period. The results of a one dimensional particles dynamic model support coagulation as the mechanism responsible for the rapid aggregate formation and the development of the V_T subsurface maxima. Comparison with KEOPS1, which investigated the same area during late summer, and previous iron fertilization experiments highlights physical aggregation as the primary mechanism for large particulate production during the earlier phase of iron fertilized bloom and its export from the surface mixed layer.

1 Introduction

Biological particle production and sedimentation out of the euphotic layer to underlying waters is the major mechanisms for atmospheric CO_2 removal and the redistribution of carbon and associated nutrients in the ocean. The fate of this exported particulate carbon is a function of the plankton community producing them in the upper layer and particle transformation by microbes and zooplankton during their descent to the deep

BGD
11, 4949–4993, 2014

sea. Physical aggregation of particles is a key process in this transformation and transport and can explain the rapid formation and export of large particles.

The Southern Ocean is the largest High Nutrients Low Chlorophyll (HNLC) region of the global ocean. However, several areas in this biological desert display strong seasonal phytoplankton blooms. Since the HNLC regions result from low supplies of the crucial nutrient iron, the hypothesis is that these blooms are supported by natural sources of iron, most likely supplied from local islands and shallow sediment (Moore and Abbott, 2002; Tyrrell et al., 2005; Blain et al., 2007; Pollard et al., 2007).

The impact of iron on the biological carbon pump has been investigated in these natural bloom regions (Blain et al., 2007; Pollard et al., 2007) and in patches formed by adding iron to localized HNLC regions (Boyd et al., 2000, 2004; Gervais et al., 2002; Buesseler et al., 2004, 2005; de Baar et al., 2005; Hoffmann et al., 2006; Smetacek et al., 2012; Martin et al., 2013). The observations made during the natural iron fertilization programs KEOPS1 and CROZEX (CROZet natural iron bloom and EXport experiment) documented a two-fold greater carbon export flux downward from the mixed layer (ML) in the natural iron fertilized bloom relative to that in unfertilized surrounding waters (Jouandet et al., 2008, 2011; Savoye et al., 2008; Pollard et al., 2009). An increase in POC flux after artificial fertilization experiments was detected only during SOFex (Southern Ocean Fe Experiment, Buesseler et al., 2005) and EIFEX (European Iron Fertilization Experiment, Smetacek et al., 2012). Optical examination of particles trapped in polyacrylamide gels during KEOPS1 found that export was dominated by fecal pellets and fecal aggregates (Ebersbach and Trull, 2008) which can be considered as a form of indirect export. By contrast, the CROZEX experiment suggested direct export of surface production by a diverse range of diatoms (Salter et al., 2007) supporting the role of phytoplankton aggregation in enhancing particulate flux. The lack of phytoplankton aggregation due to insufficient biomass has been invoked as the reason for which carbon export flux in SOIREE (Southern Ocean Iron Release Experiment) were not enhanced (Waite and Nodder, 2001; Jackson et al., 2005). The different results for these systems reflect differences in physical forcing factors, experimental duration,

BGD
11, 4949–4993, 2014

and seasonal evolution of the biological community. Because of the complexity of the export system, there are still extensive unknowns about the effect of iron fertilization on carbon export from the surface to the bottom layer.

The aim of our study is to investigate processes responsible for the formation of large particles (> 52 µm) at a short time scale during bloom development in the surface ML. We combine vertical profiles of large particles size spectra obtained during KEOPS2 with a particle dynamics model that combines phytoplankton growth and coagulation as function of size. We examined vertical profiles of particle abundances and size distributions obtained from the Underwater Vision Profiler (UVP) deployment at one bloom station above the Kerguelen plateau under pre-bloom conditions and at an early bloom stage, based on high sampling frequency during a time period of rapid change.

The coagulation model used here is an extension of a zero-dimensional model that simulates abundances of phytoplankton cells in the surface mixed layer as well as the size distributions of settling particles (e.g., Jackson et al., 2005; Jackson and Kiørboe, 2008). Here it has been extended into a one-dimensional model to describe the vertical distribution of phytoplankton in the mixed layer and the formation, distribution, and flux of aggregates.

The comparison between observed and modelled particle size distribution provides a unique opportunity to test the usefulness of the coagulation theory to explain rapid formation of large aggregates during the early stage of a phytoplankton bloom.

2 Material and methods

2.1 Field measurements

The station A3 (50°38′ S, 72°05′ E), located above the Kerguelen plateau, is characterized by a weak current (speed < 3 cm s^{-1}, Park et al., 2008b), which results in a water mass residence time of several months. This long residence time allows the bloom to

BGD
11, 4949–4993, 2014

develop and persist over an entire season in response to natural iron fertilization (Blain et al., 2007).

During KEOPS2, Station A3 was first sampled during pre-bloom conditions on 21 October 2011 (A3-1), and this site was revisited during the early bloom from 15 to 17 November (A3-2), 2 weeks after the bloom had started. The high sampling frequency during the second visit started at midnight on 15 November (Table 1).

The Underwater Vision Profiler 5 (UVP 5 Sn002) used in the present study was a component of the rosette profiler system. The UVP5 detects and measures particles larger than 52 µm on images acquired at high frequency (Picheral et al., 2010). Images were taken and data recorded at a frequency of 6 Hz, corresponding to a distance of 20 cm between images at the 1 m s^{-1} lowering speed of the CTD. The recorded volume per image is 0.48 dm^3; the total volume sampled for the 500 m depth profiles at Station A3 was 1.2 m^3. The instrument takes a digital picture of a calibrated volume lit from the side. The image is scanned for particles, and particle dimensions are measured. The pixel surface area (S_p) for each object is converted to cross-sectional area (S_m) using the calibration equation $S_m = 0.00018 S_p^{1.452}$. An equivalent spherical diameter d is calculated for that cross-sectional area.

Hydrographic and biogeochemical properties, including density, fluorescence, turbidity (as determined by a transmissometer using a wavelength of 660 nm and a 25 cm path length), were measured simultaneously with a conductivity-temperature-depth system (Seabird SBE-911+CTD) linked to a Seapoint Chelsea Aquatracka III (6000 m) chlorophyll fluorometer and a WET Labs C-Star (6000 m) Transmissiometer.

We also present selected results of chlorophyll *a* (Chl *a*) and nitrate concentrations, as well as relative biomass of different phytoplankton size classes. Chl *a* and pigment concentrations were measured using high performance liquid chromatography (HPLC) following the method described in Lasbleiz et al. (2014); the fraction of a phytoplankton group relative to the total biomass was calculated using the model of Uitz et al. (2006). Nitrate was analysed with a Technicon autoanalyzer as described in Tréguer and Le Corre (1975).

BGD
11, 4949–4993, 2014

2.2 Data processing

The particles in each 5 m depth interval, with depth determined from the associated CTD measurements, were sorted into 27 diameter intervals (from 0.052 to 27 mm, spaced geometrically), and concentrations calculated for each diameter and depth interval. We further analyzed size spectra having a minimum of 5 particles per size bin and depth interval; this criterion eliminated bins with $d > 1.6$ mm. The depth distributions of particles are summarized in terms of their total number N_T (# L^{-1}) and volume V_T ($mm^3\,L^{-1}$ = ppm) concentrations.

Particle number distributions (n) were calculated by dividing the number of particles (ΔN) within a given bin by the width of the ESD bin (Δd) and the sample volume. The resulting units are # cm^{-4}. The distributions are usually plotted in a loglog plot because of the large ranges in n and d. To compensate for these ranges, the results are often displayed as nVd spectra, where n is multiplied by the median diameter (d) for the particle size range and the spherical volume $V = \pi/6d^3$. This form of the particle size distribution has the advantage that the area under the curve is proportional to the total particle volume concentration when nVd is plotted against $\log(d)$.

The carbon export flux F_{POC} (mg C m^{-2} d^{-1}) can be estimated from the size spectra using the empirical relationship:

$$F_{POC} = Ad^b \quad (1)$$

where d is the diameter in mm, $A = 12.5$ and $b = 3.81$ (Guidi et al., 2008). Guidi et al. (2008) developed the relationship by comparing particle size spectra to sediment trap collection rates at locations around the world. The value of b is less than the value of 5 expected for spherical particles of constant density (for which mass increases as d^3, and sinking speed as d^2). It is expected for marine aggregates with increasing porosity for increasing size (e.g., Alldredge and Gotschalk, 1988).

BGD
11, 4949–4993, 2014

2.3 Model equations and parameterization

The biological model describes the growth rate of phytoplankton in the water column as a function of light and nutrient (nitrate) concentration. The model uses a maximum phytoplankton specific growth rate $G_{max} = 0.45\,d^{-1}$ (Timmermans et al., 2004; Assmy et al., 2007). Phytoplankton cells are transformed into aggregates by differential settling and shear using the standard coagulation model of Jackson (1995). Aggregates are also fragmented in two similar parts using size-dependent disaggregation rates (Jackson, 1995). The primary phytoplankton cells are chosen to match the size of *Fragiliaropsis kerguelensis* which was the dominant species under pre-bloom conditions (Armand et al., 2014). A single phytoplankton cell has $d_1 = 20\,\mu m$, a density $1.0637\,g\,cm^{-1}$, and a resulting settling speed $v_1 = 1.05\,m\,d^{-1}$. The probability that two particles colliding stick together, α, is assumed to be 1. The average turbulent shear rate is $\gamma = 1\,s^{-1}$ (Jackson et al., 2005). The initial abundance of phytoplankton is 10 cells cm^{-3}. These and other parameter values are shown in Table 2.

The one-dimensional model simulates the distribution of particles of different sizes, including solitary phytoplankton cells, and nitrate concentrations at 2 m depth intervals within the 0–150 m layer. This depth range corresponds to the average surface ML thickness during the survey (Table 1). Neither zooplankton grazing nor particle transformation by bacterial processes are included in these simulations. The model is described in greater detail in Appendix A.

While the concept of spherical diameter is simple for a solid sphere, it is not for irregular marine aggregates, with different shapes, assembled from multiple sources, having water in the interstices between their components and yielding different sizes for different measurement techniques (e.g., Jackson, 1995). The simplest diameter is the conserved diameter d_c, the diameter if all the solid matter was compressed into a solid sphere. It has the advantage that when two particles collide and form a new particle, the conserved volume of the new particle is the sum of the conserved volumes of the two colliding particles. The particle diameter d determined by the UVP is larger than

BGD
11, 4949–4993, 2014

d_c because aggregate size is determined from the outer shape of the aggregate and thus contains pore water between source particles. The relationship between the two measures of particle diameter is described using the fractal dimension (see Appendix A). The model calculations use d_c. However, all model results shown here use the apparent diameter d_a, which is used to approximate the diameter reported by the UVP. The value of d_a is calculated from d_c using the fractal relationship and a fractal dimension of 2 (Appendix A). Note that reported values of the fractal dimension vary widely, from 1.3–2.3 (Burd and Jackson, 2009). The value of 2 used here is in the middle of this range and yields peaks in the nVd distributions similar to those determined from UVP measurements, unlike values of 2.1 and 1.9 (not shown).

3 Results

3.1 Observations

3.1.1 Biogeochemical and physical context

The water column was characterized by a deep mixed layer (~ 150 m) during the pre-bloom and early bloom surveys, with a range of 120 to 171 m (Figs. 1 and 2). Isopycnal displacements of up to 50 m can be seen in the density profiles. Such vertical movements are known to result from semi-diurnal internal tides in this region (Park et al., 2008a).

The fluorescence and Chl *a* concentrations show a 4-fold increase from A3-1 (21 October) to A3-2 (15–17 November), with Chl *a* concentrations at the surface increasing from 0.5 to ~ 2 $\mu g L^{-1}$ (Figs. 1 and 2). The Chl *a* profile determined using bottle samples for station A3-2 was characterized by a subsurface maximum at 170 m, at the bottom of the mixed layer (Fig. 3). The chlorophyll profiles determined using the in situ fluorometer were either relatively constant or had maxima at 50 m or shallower (Figs. 1 and 2). Variations in the maximum depth of fluorescence from the in situ profiles were

BGD
11, 4949–4993, 2014

associated with temporary deepening of the mixed layer at 7.50 a.m. and 7.15 p.m. on 16 November and at 5.30 a.m. on 17 November.

In the surface mixed layer, the beam attenuation coefficient (turbidity) had a similar distribution as fluorescence (Figs. 1 and 2). The two were, in fact, highly correlated in the surface mixed layer (r = 0.95), which was not always the case in deeper layers. Nitrate concentrations at A3-1 were 28 to 30 µM in the mixed layer, and then decreased by 4 µM at A3-2 (Fig. 3a).

Pigment analysis (Fig. 3) and cell counts of phytoplankton captured in nets (Armand et al., 2014) showed that the phytoplankton community was dominated by diatoms, *Fragilariopsis* at A3-1 and an assemblage of *Fragilariopsis*, *Chaetoceros* and *Pseudo-nitschia* at A3-2. The zooplankton community was dominated by copepods with a mixture of adult (50.5 %) and copepodites stage (49.5 %) at A3-2 (Carlotti et al., 2014). Zooplankton biomass increased from 1.4 g C m^{-2} at A3-1 to 4.1 g C m^{-2} at A3-2 over the 0–250 m layer, and was thus more than 2 fold lower than the biomass measured in summer during KEOPS1 (Carlotti et al., 2008).

3.1.2 Evolution of the total abundance and volume distributions in the mixed layer

In the pre-bloom profile, total particle abundance (N_T) and volume (V_T) distributions at station A3 were characterized by a two layers structure (Fig. 1b). The shallower layer had relatively uniform N_T (V_T) values of 90 ± 5 particles L^{-1} (0.3 ± 0.1 $mm^3 L^{-1}$) between 0 and 100 m; the second layer, from 100 m to the base of the ML (166 m), had subsurface N_T and V_T maxima of 142 particles L^{-1} and 0.45 $mm^3 L^{-1}$.

There was a two-fold increase in N_T at the first cast of the early bloom (A3-2/1), with values reaching 200 ± 7 # L^{-1} in the first hundred meters and a subsurface maximum of 300 # L^{-1} (Fig. 4). V_T also increased by one order of magnitude reaching a value of 3 $mm^3 L^{-1}$ at the depth of the subsurface maxima (Fig. 4). There was a 40 m thick surface layer with constant N_T and V_T and a subsurface maximum that was also present in

BGD
11, 4949–4993, 2014

subsequent casts but at variable depths. Particularly striking was the rapid and continuous increase of both N_T and V_T from A3-2/1 to A3-2/5 over a roughly 24 h time period. This was more than a redistribution of aggregates, as N_T and V_T integrated over the ML increased from 282 to 743 # m^{-2} and from 101×10^3 to 1500×10^3 $mm^3\,m^{-2}$. There was a further increase in the maximum V_T to 25 $mm^3\,L^{-1}$, almost by two orders of magnitude compared to the pre bloom situation, by the end of the survey.

3.1.3 Evolution of size distributions with depth and time during the early bloom time series

The particle size distributions (PSD) calculated from the UVP observations provide additional insight to the change in particle abundance over the two days spring observation period. In order to display the vertical structure of PSD, we compare the average over the nominal euphotic zone (0 to 40 m) to the average over the 40 m centered on the subsurface particle maximum. Particles larger than 129 µm were more abundant in the subsurface layer (Fig. 5a). Consistent with the analysis in the previous section, the smallest difference between the 2 layers occurred during the pre-bloom sampling (A3-1). The maximum increase was seen for the 0.128 to 0.162 mm and 0.204 to 0.257 mm size classes, with abundance increase of 66 # L^{-1} and 62 # L^{-1} respectively at A3-2/3 (16 November 2011 – 11.30 a.m.). The increase was also substantial in the 0.4–0.5 mm size range. The cumulative volume distribution shows that increased particle volumes resulted from formation of larger particles in the 0–40 m euphotic zone (Fig. 5b).

Regarding the temporal variation at the depth of maxima: half of V_T was in particles with $d > 0.5$ mm at the start of the survey, while these larger particles provided more than 80 % at the end. The largest change in size spectra was between morning (A3-2/2) and the middle of the night (A3-2/5) of 16 November.

The nVd size distribution for profile A3-2/5 is shown in detail in Fig. 6. The area under the curve at a constant depth is proportional to the particle volume V_T at that depth. Between the surface and 60 m most particle volume is in the smallest size class with particles d ranging between 200 and 500 µm. Massive changes occurred with depth

BGD
11, 4949–4993, 2014

with an increase of the volume and d. The volumes from 60 m to 150 m are supported by larger particles ranging between 0.65 mm to 1.1 mm, with a peak of 30 ppm for a d of 1 mm.

3.1.4 Particle distributions below the ML

In the first 50 m below the ML, V_T values mirrored those in the overlying waters, increasing to 20 ppm by the end of the survey period (A3-2/7) (Fig. 7). The vertical decrease in V_T from the base of the ML to 200 m was about a factor of 20 for A3-2/6 and A3-2/7.

Below 200 m, the depth limit for winter mixing, there was no change in V_T during the two days survey. The average V_T was 0.40 ± 0.10 and $0.38 \pm 0.10\,mm^3\,L^{-1}$ at respectively 250 and 350 m. There was an increase in V_T at about 475 m caused by resuspension from the bottom, as documented during KEOPS1 (Chever et al., 2010; Jouandet et al., 2011).

The particle number distribution (n) decrease from the base of the mixed layer to 350 m was observed in all size classes and mostly for particles larger than 500 µm which were not anymore detected (Fig. 7b).

3.1.5 Relationship between particle volume and fluorescence

As previously mentioned, there was no simple correlation between V_T and fluorescence. However, separating the observations by depth layers (the mixed layer, the base of the ML to 200 m and deeper than 200 m) reveals a pattern (Fig. 8). In the shallowest layer, there was an increase from the pre-bloom values of low fluorescence and particle volume for A3-1 (21 October) to high fluorescence and low particle volume for A3-2/1 (15 November, 11.20 p.m.). This is consistent with an increase in phytoplankton biomass but no aggregate production. For A3-2/2, there are hints of an increase of V_T, which became pronounced in subsequent casts. The increased particle concentrations were accompanied by a slight decrease in fluorescence. For the seven casts

BGD
11, 4949–4993, 2014

performed during the early bloom stage, the correlations between fluorescence and V_T were negative (−0.53), with a slope of −0.015 µg Chl mm^{-3}.

In the second layer, immediately below the surface mixed layer, fluorescence and V_T increased together, with a positive correlation coefficient (0.68) and a slope of 0.036 µg Chl mm^{-3} (Fig. 8). This is consistent with no phytoplankton growth in this depth layer, but with phytoplankton and aggregates arriving together from above. There was no correlation between fluorescence and V_T below 200 m.

3.1.6 POC flux

The flux at 200 m computed from the UVP particle size distributions increased from 1.8 mg m^{-2} d^{-1} during pre-bloom conditions to 23 mg C m^{-2} d^{-1} during the early bloom (last cast of the survey). This increase over time as observed from UVP measurements persisted at 400 m but with a smaller value, F_{POC} increasing from 1.04 to 3.5 mg C m^{-2} d^{-1} at 400 m (Table 3).

Our POC flux estimates at 200 m for spring are in the range of the POC flux estimated from the sediment trap PPS3/3 (27 ± 8 mg m^{-2} d^{-1}) and below the estimate made from the gel trap (F_{POC} = 66 mg C m^{-2} d^{-1}) and from the thorium deficit ($F_{POC\text{-}Th}$ = 32 mg m^{-2} d^{-1}) (Laurenceau et al., 2014; Planchon et al., this volume). $F_{POC\text{-}Th}$ at 100 m increased from pre-bloom to early bloom but stayed unchanged at 200 m. The $F_{POC\text{-}Th}$ at 200 m was estimated at A3-2/1, and this result is consistent with UVP observations that did not record any V_T increase.

3.2 Simulations

3.2.1 Development of the phytoplankton bloom

The phytoplankton in the model grew exponentially in the upper part of the water column for the first eight days of the simulation, slowing down as light limitation became important (Fig. 9a). The specific rate of integrated population growth (0 to 150 m) was

BGD
11, 4949–4993, 2014

$\sim 0.06\,d^{-1}$ for this initial period. The peak phytoplankton biomass was 2 µg Chl L^{-1} at about 10 m depth on day 13. The phytoplankton biomass decreased slightly when coagulation became an important removal mechanism by day 20, with surface phytoplankton biomass of 1.7 µg Chl L^{-1}, a maximum concentration of 1.9 µg Chl L^{-1} at 15 m, and a minimum concentration of 0.2 µg Chl L^{-1} at 150 m. Surface nitrate concentrations decreased from the initial 30 to 25 µM by day 20 (Fig. 9b).

3.2.2 Development of the aggregate volume

Aggregates with $d_a > 100$ µm appeared by day 14, when the total volume peaked at 1.3 ppm at 40 m (Fig. 9c). As the phytoplankton biomass increased, the maximum total volume also increased. The depth of the aggregate maximum deepened as the aggregates sank, becoming 17 ppm below 140 m on day 18.5. By day 20, the initial rapid coagulation phase ended, with the maximum phytoplankton biomass decreasing slightly in the upper 50 m and the aggregates at the base of the mixed layer slowly decreasing.

The vertical size distribution at day 20 provides further details on the system (Fig. 10). The nVd_a size distribution shows the distribution of particle volume, with the area under the curve being proportional to the particle volume when displayed with a logarithmic d_a axis, as here (Fig. 10). Most particle volume at the surface is in the smallest particles, the single phytoplankton cells. At 10 m depth, aggregates appear with a maximum nVd_a value at $d_a = 200$ µm. With increasing depth, the total volume and the diameter of the maximum d_a both increase. The maximum d_a became 0.9 mm at about 70 m depth, remaining constant with increasing depth, even though the total volume continued to increase with depth.

BGD
11, 4949–4993, 2014

4 Discussion

The rapid production of aggregates at station A3 observed in this study provides a dramatic example of the importance of coagulation in controlling PSD and vertical export of primary production. It is also striking how well the results of our simulation of the phytoplankton bloom and consequent coagulation match the observations. KEOPS2 did not fit the standard epipelagic/mesopelagic paradigm because the ML is 150 m, and thus much deeper than the euphotic zone (30–40 m). Thus, much of the aggregate production occurred in the upper mesopelagic zone.

4.1 Correspondence between observations and coagulation-based model

4.1.1 Critical concentration

Coagulation theory has been used to predict the maximum phytoplankton biomass in the ocean (e.g., Jackson and Kiørboe, 2008). Coagulation of phytoplankton cells is a non-linear process. Rates increase dramatically as phytoplankton biomass increases, eventually removing cells as fast as they divide. The volume concentration at which this occurs is the critical volume concentration (Jackson, 2005):

$$V_{cr} = \pi\mu(8\alpha\gamma)^{-1} \quad (2)$$

For this calculation, we assume an average specific growth rate for the population increase rate $\mu = 0.1\,d^{-1}$, in agreement with measurements made by Closset et al. (2014), $\alpha = 1$, and $\gamma = 1\,s^{-1}$. Note that the average increase rate is not the same as the peak rate G_{max}. For a POC: volume ratio of $0.17\,g\,C\,cm^{-3}$ (Jackson and Kiørboe, 2008) and a carbon to chlorophyll ratio of 50 g C : g Chl, this is equivalent to 1.5 µg Chl *a* L^{-1}. This value for V_{cr} is remarkably close to the maximum concentrations of 2–2.2 µg Chl *a* L^{-1} observed during the particle formation at A3-2.

BGD
11, 4949–4993, 2014

4.1.2 Similarities between observations and simulations

There are also several striking correspondences between the observations at A3 during KEOPS2 and the more sophisticated one-dimensional coagulation model used here. In the model, the transition to rapid coagulation took place when relatively little of the initial nitrate had been consumed, a decrease of 4.8 µM at the surface relative to that at 150 m. The actual surface concentration of nitrate for A3-2/5 was 25.2 µM, and thus 3.6 µM lower than the value at A3-1. In addition, the transition from non-coagulated to coagulated states was rapid, taking less than 2 d in both the model and the observations. Also striking is the similarity in the shape of the nVd spectra at the base of the mixed layer, centred at 0.9 mm for the model and 1 mm for the observations, with half widths of 1 mm for the model and 0.6 mm for A3-2/5.

The aggregate mass : volume ratio in the model varies with aggregate size, as well as fractal dimension, because of the increase in porosity with size. At the base of the mixed layer, the standard model predicts a ratio 0.1 µg Chl mm^{-3}; the value drops to 0.006 µg Chl mm^{-3} if the simulation is modified so that aggregates have a fractal dimension of 1.8. Again, the model and observations agree.

The nature of the exported material collected in a free drifting sediment gel trap at 210 m supports the importance of algal coagulation in forming the exported material (Laurenceau et al., 2014). Their analysis shows that the particle flux number and volume were dominated by phytoaggregates over the 0.071–0.6 mm size range.

4.1.3 Differences between observations and simulations

There are, not unexpectedly, differences between model results and observations. Possibly most noticeable are the relatively constant observed fluorescence profiles through the surface mixed layer, but the pronounced shallow subsurface chlorophyll maximum in the model. Increased mixing in the model would smooth the chlorophyll profiles, as well as the distribution of particle volume. Simulations made using a much larger mixing coefficient (1000 $m^2 d^{-1}$) yield a smaller difference in chlorophyll between the

BGD
11, 4949–4993, 2014

surface and 150 m, but there is still a difference of 0.8 µg Chl L^{-1} (results not shown). The vertical mixing rate estimated for the iron fertilization experiment EIFEX was actually smaller, 29 $m^2 d^{-1}$ (Smetacek et al., 2012). Whatever the reason for the relatively uniform fluorescence profile, it is not simply a faster diffusive mixing rate.

In a model such as the one used in the present study, there are many parameters that influence the final results. These include the fractal dimension, the size of the phytoplankton cells, how diatom chains are described, disaggregation rates, and presence of grazers. While the parameters could be tuned to give an improved fit, what is striking is the similarity between observations and the model without such a fitting procedure.

Other processes are known to affect particle concentrations and fluxes, most notably zooplankton fecal pellet production (e.g., Lampitt et al., 1993; Stemmann et al., 2000; Turner et al., 2002). The abundance and volume of zooplankton larger than 0.7 mm were estimated from the identification of organism in the vignettes recorded by the UVP using the Zooprocess imaging software (see Picheral et al., 2010). The volume of copepods did not increase through the early bloom survey, suggesting that they were not responsible for the observed rapid increase in particles. In addition, fecal pellet production should have a diurnal signal (Carlotti et al., 2014), which was not observed in the V_T profiles. Ingestion rates were also estimated from zooplankton biomass using the relationship detailed in Carlotti et al. (2008) using the biomass results integrated over the 0–250 m layer. The ingestion rate was 1.36 mg C d^{-1} during the early bloom cast and lower than during the KEOPS1 summer cruise. Lastly, fast sinking fecal pellets are much smaller than the aggregates observed here. For example, fecal pellets falling at 100 m d^{-1} are typically 2–5 × 10^6 µm^3, equivalent to d = 200 µm (Small et al., 1979), compared to the mm sized aggregates dominating at A3. Thus, changes in zooplankton populations can be ruled out to explain the observed V_T increase. We also classified objects larger than 0.7 mm in the vignettes as either aggregates or fecal sticks/pellets and aggregates dominated the particles abundance between 0–200 m.

BGD
11, 4949–4993, 2014

4.2 Comparison with other studies

4.2.1 KEOPS 1

The comparison of our results with the size spectra obtained from UVP measurements during the peak and the late stage of the bloom at Station A3 (KEOPS 1) allows us to investigate the seasonal variability of particle production in the 0–200 m layer and the POC export flux (Fig. 11, Table 3).

During summer (KEOPS1), the phytoplankton community was also dominated by *Chaetoceros* but shifted to *Eucampia antarctia* by the end of the bloom (Armand et al., 2008). Zooplankton abundance was 10-fold higher than during the early bloom and the community was dominated by copepods at copepodite stage. The mixed layer decreased from 150 m during early bloom to 70 m during summer.

During KEOPS 2, V_T increased more than 20-fold from pre-bloom conditions to the early bloom as a result of the higher diatom biomass (Armand et al., 2014). The value of V_T achieved by the time of the bloom decline in February (KEOPS1) was quite similar to that measured during early bloom for KEOPS2 but the vertical structure was different, with two subsurface maxima during KEOPS1, the first one present at the base of the ML (70 m). The larger V_T measured in January was associated with an increase in the fraction of large particles (Fig. 11c).

Below 200 m depth, V_T was still 10 times higher during the peak bloom as compared to early bloom. This resulted in 40- (at 200 m) and 10-fold (at 400 m) higher carbon export fluxes during the peak bloom than the early bloom (Table 3). During the decline of the bloom, V_T and POC flux were still higher than during early bloom. This is consistent with the general scheme of low production – high export at the end of the bloom put forward by Wassmann (1998).

Our results provide seasonal insights to aggregate formation and export. The early bloom occurs before zooplankton grazing dominates. This leads to a large increase in diatom abundance resulting in rapid aggregate formation and export from the surface ML. Later in the season, export becomes controlled by zooplankton grazing and fe-

BGD
11, 4949–4993, 2014

cal pellet production as found from the gel trap analysis (Ebersbach and Trull, 2008). Despite the importance of zooplankton grazing in the late season, the presence of V_T maxima at the base of the ML indicates that coagulation still occured during summer.

An increase of aggregate formation through coagulation as result of high cell numbers in the ML and their disappearance due to grazing between the base of the mixed layer and 200 m traps could also explain the dominance of fecal aggregates in the gel traps during the summer deployments.

4.2.2 Possible impact of artificial iron fertilization on coagulation

Our results can be compared to those from other iron fertilization experiments to understand the role of coagulation for particle export. However, we want to point out that these fertilization experiments differ in several aspects, such as location, physical and chemical regimes and the techniques applied to determine stocks and fluxes. In addition, conclusions about carbon export from the surface often depend on sediment traps that are usually located well below the euphotic zone or surface ML. With this preamble, we compare our results to those from other iron fertilization studies.

The artificial iron fertilization experiment SOIREE (February 1999) has highlighted an increase in phytoplankton biomass (Chl $a = 2\,\mathrm{mg\,m^{-3}}$) as a result of the iron addition, but no rapid removal of phytoplankton production. The export flux was low and driven by phyto-detrital aggregates (Waite and Nodder, 2001). Jackson et al. (2005) argued that the final abundance of phytoplankton cells was too low to cause rapid coagulation and sinking. There was also a change in diatom settling rate associated with a change in the abundance of phytoplankton cells. The persistence of the bloom after iron was depleted suggested that zooplankton grazing was not removing the particulate material either.

The EIFEX (February–March 2004) environmental system was remarkably similar to that of KEOPS2 (Smetacek et al., 2012). The mixed layer was slightly shallower during EIFEX (100 m) than during KEOPS2 (150 m) but still relatively deep; the phytoplankton accumulation rates were also similar (0.03 to $0.11\,\mathrm{d^{-1}}$). Iron fertilization

BGD
11, 4949–4993, 2014

stimulated a large diatom bloom that reached phytoplankton biomass of about 2 mg Chl $a\,m^{-3}$ four weeks after the fertilization started. There was little effect on vertical export during the first four weeks, and export rapidly increased thereafter from about 25 to 110–140 mmol C $m^{-2}\,d^{-1}$. This was associated with mass mortality of several diatom species that formed rapidly sinking, mucilaginous aggregates of entangled cells and chains (Smetacek et al., 2012).

CROZEX investigated the impact of high biomass (Chl $a = 2\,mg\,m^{-3}$) during 2 legs (November 2004 and January 2005) associated with the bloom decline on carbon export (Venables et al., 2007). Carbon export fluxes estimated from a sediment trap in the highly productive naturally iron fertilized region of the sub-Antarctic waters were two to three times larger than the carbon fluxes from adjacent HNLC waters (Pollard et al., 2009). The organisms and material involved in export were directly measured using a novel drifting sediment trap PELAGRA (Salter et al., 2007) and export was dominated by a diverse range of diatoms suggesting an important role for direct export.

The SAZ-Sense project examined the particulate flux from the PPS3 and gel trap in a region of elevated biomass (Chl $a = 1.9\,mg\,m^{-3}$) in the Sub Antartic Zone east of Tasmania fuelled by enhanced iron supply during summer (January–February 2007). The gel traps were at 140, 190, 240, and 290 m depths. The analysis of the export material shows that fecal aggregates dominated the flux at all sites (Ebersbach et al., 2011).

The LOHAFEX iron fertilization experiment was one of the few to use a particle measuring system, also the UVP (Martin et al., 2013). Just as did EIFEX, a cyclonic eddy on the Antarctic Polar Frontal Zone was fertilized with iron. In LOHAFEX, the water was low in silica. There was almost a doubling of phytoplankton biomass to 1–1.5 mg Chl $a\,m^{-3}$, but 90 % of the biomass was in flagellates less than 10 µm rather than in diatoms. There was no observable change in concentrations of particles larger than 100 µm or of vertical particle flux. There were several reasons proposed for the low export, including the lack of diatoms in the low silicate water and intense particle consumption, particularly at the base of the mixed layer (66 m). We note that the maximum Chl *a* concentration

BGD
11, 4949–4993, 2014

($1.5\,mg\,m^{-3}$) was also lower than that achieved in EIFEX ($2.5\,mg\,m^{-3}$) and KEOPS2 ($2.2\,mg\,m^{-3}$), fertilization studies that had a strong indication of export flux driven by coagulation.

Thus, there is much corroboration to the conclusion that coagulation is a primary mechanism for particulate production during a phytoplankton bloom and more specifically during the early phase and its export from the surface mixed layer.

5 Conclusions

It is clear that particle flux in the ocean is the result of many interacting processes, and none of these has been identified dominant across systems. In the present study, we were able to document one process that is rapid aggregate formation and sedimentation of high concentrations of diatoms. Our observations are consistent with results from a one-dimensional coagulation model. Our results demonstrate the utility of coagulation theory in understanding the vertical flux and its importance to initiate the formation of large particles in the mixed layer and their subsequent transfer to depth. Nevertheless efforts are still required to better understand vertical variations at a fine scale and particularly to estimate the role of grazing in decreasing the total particle volume in the pycnocline.

Appendix A

Model description

The biological model for phytoplankton growth is a modified form of that in Evans and Parslow (1985) and Fasham et al. (1990). In this case, there is only one nutrient, nitrate, and phytoplankton are lost to coagulation as in Jackson (1995) and Jackson et al. (2005). There are no grazing losses. Values for constants are given in Table 1.

BGD
11, 4949–4993, 2014

A1 Nitrate concentration

Change in nitrate concentration N:

$$\frac{\partial N}{\partial t} = K_z \frac{\partial^2 N}{\partial z^2} - G\phi \tag{A1}$$

where K_z = vertical mixing coefficient, G is the phytoplankton specific growth rate, and φ is the phytoplankton concentration.

A2 Phytoplankton growth

Phytoplankton growth rate at any given irradiance and nutrient concentration is given by

$$G = G_{\max} \min(r_p, r_n) \tag{A2}$$

where $G_{\max}$ is the maximum specific growth rate, r_p and r_n are the relative growth rates possible growth for photosynthesis and nutrient limitation at I and N. They are calculated by

$$r_p = \frac{\alpha_I I}{\sqrt{\alpha_I{}^2 I^2 + G_{\max}^2}} - \frac{r}{G_{\max}} \tag{A3}$$

where r is the phytoplankton loss rate and α is the slope of the PI curve.

$$r_n = \frac{N}{K_D + N} \tag{A4}$$

where K_D is the half saturation constant for nitrate uptake.

Irradiance I given by

$$I = I_0 e^{\int_0^z k dz} \tag{A5}$$

BGD
11, 4949–4993, 2014

where I is the surface irradiance, $k = k_w + \varphi k_r$, k_w is the attenuation coefficient for water equal to $0.04\,m^{-1}$, and k_r is the light absorption coefficient for q plants. The value of k_r was chosen so that k equaled the observed attenuation at A3 ($k = 0.048\,m^{-1}$ for $P = 0.6\,\mu g\ chl\ L^{-1}$). Surface irradiance was calculated using the relationships of Evans and Parslow (1985) for a latitude of 50° S and a starting time 120 d after winter solstice.

A single phytoplankton cell was assume to have a diameter of 20 µm and a density of $1.0637\,g\,cm^{-3}$ (compared to a fluid density of $1.0275\,g\,cm^{-3}$), for a resulting settling speed of $1.05\,m\,d^{-1}$.

A3 Describing particle size distributions

Standard coagulation theory describes particle size distributions using a number spectrum $n(s)$, where s is particle size, such as mass m or equivalent spherical diameter d. Number spectra in terms of m and d can be related

$$n(d) = n(m)\frac{dm}{dd} \tag{A6}$$

The total number of particles in a small size interval $d_l < d \le d_l + \Delta d$ is approximately $n\Delta d$. For a sufficiently small Δd, all particles have the same individual volume $V(d) = \frac{\pi}{6}d^3$. The total particle volume in the interval is then $V(d)n\Delta d$. The total particle volume for any large particle range $d_l < d \le d_u$ is

$$V_T = \int_{d_l}^{d_u} V(d)n(d)dd \tag{A7}$$

which is proportional to the area under the curve when nV is plotted as a function of d. Plotting nV vs. the logarithm of d destroys the relationship between the area under the curve and the total particle volume; plotting nVd as a function of log d restores it. We will discuss particle size distributions in terms of the nVd form of the distribution, but note that it contains the same content as n.

BGD
11, 4949–4993, 2014

A4 How coagulation changes size distributions

Coagulation destroys small particles and creates new ones in a way that is mathematically expressed as

$$\frac{\partial n(m,t)}{\partial t} = +\alpha \int_0^m n(m_1)\, n(m-m_1)\, \beta(m_1, m-m_1)\, dm - \alpha n(m) \int_0^\infty n(m_1)\, \beta(m, m_1)\, dm_1 \tag{A8}$$

where $\beta(m_1, m_2)$ is the coagulation kernel and describes the collision rate between particles of masses m_1 and m_2 and α is the stickiness, the probability of a collision destroying the two colliding particles and forming a larger particle.

One of the techniques for solving this equation numerically is to break the size distribution n into segments, called sections, each with a fixed shape but a variable magnitude, such that

$$n(m,t) = \frac{Q_i(t)}{\hat{m}_{l-1} m} \tag{A9}$$

within a range of $\hat{m}_l > m \geq \hat{m}_{l-1}$, where $Q_i(t)$ is the total particulate mass within the bounds (e.g., Jackson, 1995) and the range represents the section boundaries. This approximation breaks $n(m,t)$ into separate time and mass varying parts. Gelbard et al. showed that doing so allows Eq. (A8) to be transformed from an integro-differential equation to a series of ordinary differential equations:

$$\frac{dQ_l}{dt} = \frac{\alpha}{2} \sum_{i=1}^{l-1} \sum_{j=1}^{l-1} {}^1\bar{\beta}_{i,j,l} Q_i Q_j - \alpha Q_l \sum_{i=1}^{l-1} {}^2\bar{\beta}_{i,l} Q_i - \frac{\alpha}{2} {}^3\bar{\beta}_{l,l} Q_l^2 - \alpha Q_l \sum_{i=l+1}^{l_{\max}} {}^4\bar{\beta}_{i,l} Q_i \tag{A10}$$

where ${}^1\beta_{i,j,l}$, ${}^2\beta_{i,l}$, ${}^3\beta_{l,l}$, and ${}^4\beta_{i,l}$ are sectional coefficients and $l_{\max}$ is the total number of sections. The equations simplify if the mass of the upper boundary of a section is twice that of its lower boundary.

BGD
11, 4949–4993, 2014

Jackson (1995) added a disaggregation term to Eq. (A10) which moved mass from section i to the next lower section $i-1$ at a rate $\lambda_i Q_i$, where λ_i is a size dependent disaggregation coefficient. We used the values for λ_i from Jackson (1995).

The algae were assumed to be occupy the first section: $\varphi = Q_1$. The equation describing their concentration is

$$\frac{\partial Q_1}{\partial t} = Q_1 G + v_1 \frac{\partial Q_1}{\partial z} - K_z \frac{\partial^2 Q_1}{\partial z^2} - \frac{\alpha}{2} {}^3\bar{\beta}_{1,1} Q_1^2 - \alpha Q_1 \sum_{i=2}^{I_{\max}} {}^4\bar{\beta}_{i,1} Q_i + \lambda_2 Q_2 \quad \text{(A11)}$$

For particles in larger sections, the equation describing their concentration becomes

$$\frac{\partial Q_I}{\partial t} = v_I \frac{\partial Q_I}{\partial z} - K_z \frac{\partial^2 Q_I}{\partial z^2} + \lambda_{I+1} Q_{I+1} - \lambda_I Q_I + \frac{\alpha}{2} \sum_{i=1}^{I-1} \sum_{j=1}^{I-1} {}^1\bar{\beta}_{i,j,I} Q_i Q_j$$
$$- \alpha Q_I \sum_{i=1}^{I-1} {}^2\bar{\beta}_{i,I} Q_i - \frac{\alpha}{2} {}^3\bar{\beta}_{I,I} Q_I^2 - \alpha Q_I \sum_{i=I+1}^{I_{\max}} {}^4\bar{\beta}_{i,I} Q_i \quad \text{(A12)}$$

where v_I is the settling rate for particles in the Ith section.

A5 Measures of aggregate size

Because aggregate porosity increases with size, particle density decreases as particle size increases. The relationship between the diameter assigned to a particle from analysis of an image d_a is frequently described using a fractal dimension D_f: $m \propto d_a^{D_f}$. Increasing D_f decreases the porosity of large particles and results in smaller values of d_a for a given m. An apparent volume for a sphere with diameter d_a is then $V_a = \frac{\pi}{6} d_a^3$. A conserved volume V_c can be calculated from a particle's mass and the density of the single cell. Its diameter d_c can be calculated assuming it is a sphere.

A6 Numerical solution of equations

The equations were solved numerically for a 150 m mixed layer using a centered-difference scheme, no-flux boundary conditions at the surface, fixed nitrate concentra-

BGD
11, 4949–4993, 2014

tion = 30 µM and no diffusive particle flux at the bottom boundary (150 m). Equations were solved at a vertical spacing of 2 m. Particle concentrations were calculated in terms of the conserved volume.

Parameter values are given in Table 2.

Acknowledgements. Thanks to the Kerguelen Ocean and Plateau Compared Study (KEOPS 2) shipboard science team and the officers and crew of R/V *Marion Dufresne* for their efforts. Christine Klaas provided helpful input on biological conditions. This research was supported by the French Agency of National Research grant (# ANR-10-BLAN-0614). G. A. Jackson was supported by US National Science Foundation (NSF) grant OCE99-27863. L. Stemmann was supported by the chair VISION from CNRS/UPMC.

References

Alldredge, A. L. and Gotschalk, C.: In situ settling behavior of marine snow, Limnol. Oceanogr., 33, 339–351, 1988.

Armand, L. et al.: Evolving diatom community structure and biomass in the naturally-fertilised bloom on Kerguelen Plateau, 2014.

Armand, L. K., Cornet Barthaux, V., Mosseri, J., and Quéguiner, B.: Late summer diatom biomass and community structure on and around the naturally iron-fertilized Kerguelen Plateau in the Southern Ocean, Deep-Sea Res. Pt. II, 55, 653–676, 2008.

Assmy, P., Henjes, J., Klaas, C., and Smetacek, V.: Mechanism determining species dominance in a phytoplankton bloom induced by the iron fertilization experiment EisenEx in the Southern Ocean, Deep-Sea Res. Pt. I, 54, 340–362, 2007.

Blain, S. et al.: Effect of natural iron fertilization on carbon sequestration in the Southern Ocean, Nature, 446, 1070–1074, 2007.

Boyd, P. W. et al.: A mesoscale phytoplankton bloom in the polar Southern Ocean stimulated by iron fertilization, Nature, 407, 695–702, 2000.

Boyd, P. W. et al.: The decline and fate of an iron-induced subarctic phytoplankton bloom, Nature, 428, 549–553, 2004.

Buesseler, K. O., Andrews, J. E., Pike, S. M., and Charette, M. A.: The effects of iron fertilization on carbon sequestration in the Southern Ocean, Science, 304, 414–417, 2004.

BGD
11, 4949–4993, 2014

Buesseler, K. O., Andrews, J. E., Pike, S. M., and Charrette, M. A.: Particle export during the Southern Ocean Iron Experiment (SOFeX), Limnol. Oceanogr., 50, 311–327, 2005.
Burd, A. B., Jackson, G. A., Particle aggregation, Annu. Rev. Mar. Sci., 1, 65–90, 2009.
Carlotti, F., Thibault-Botha, D., Nowaczyk, A., and Lefèvre, D.: Zooplankton community structure, biomass, and role in carbon fluxes during the second half of a phytoplankton bloom in the eastern sector of the Kerguelen Shelf (January–February 2005), Deep-Sea Res. Pt. II, 55, 720–733, 2008.
Carlotti, F. et al.: Mesozooplankton structure and functioning during the onset of the Kerguelen Bloom during KEOPS2 survey, 2014.
Chever, F., Sarthou, G., Bucciarelli, E., Blain, S., and Bowie, A. R.: An iron budget during the natural iron fertilisation experiment KEOPS (Kerguelen Islands, Southern Ocean), Biogeosciences, 7, 455–468, doi:10.5194/bg-7-455-2010, 2010.
Closset et al.: Seasonal evolution of net and regenerated silica production around a natural Fe-fertilized area in the Southern Ocean estimated from Si isotopic approaches?, 2014.
De Baar, H. J. W., Boyd, P. W., Coale, K. H., Landry, M. R., Tsuda, A., Assmy, P., Bakker, D. C. E., Bozec, Y., Barber, R. T., Brzezinski, M. A., Buesseler, K. O., Boye, M., Croot, P. L., Gervais, F., Gorbunov, M. Y., Harrison, P. J., Hiscock, W. T., Laan, P., Lancelot, C., Law, C. S., Levasseur, M., Maretti, A., Millero, F. J., Nishioka, J., Nojiri, Y., van Oijen, T., Riebesell, U., Rijkenberg, M. J. A., Saito, H., Takeda, S., Timmermans, K. R., Veldhuis, M. J. W., Waite, A. M., Wong, C- H.: Synthesis of iron fertilization experiments: from the iron age in the age of enlightenment, J. Geophys. Res., 110, 1–24, 2005.
Ebersbach, F. and Trull, T. W.: Sinking particle properties from polyacrylamide gels during KEOPS: Controls on carbon export in an area of persistent natural iron inputs in the Southern Ocean, Limnol. Oceanogr., 53, 212–224, doi:10.4319/lo.2008.53.1.0212, 2008.
Ebersbach, F., Trull, T. W., Davies, D., Moy, C., Bray, S. G., and Bloomfield, C.: Controls on mesopelagic particle fluxes in the Sub-Antarctic and Polar Frontal Zones in the Southern Ocean south of Australia in summer – perspectives from free-drifting sediment traps, Deep-Sea Res. Pt. II, 58, 2260–2276, 2011.
Evans, G. T. and Parslow, J. S.: A model of annual plankton cycles, Biol. Oceanogr., 3, 327–347, 1985.
Fasham, M. J. R., Ducklow, H. W., and McKelvie, S. M.: A nitrogen-based model of plankton dynamics in the ocean mixed layer, J. Mar. Res., 48, 591–639, 1990.

BGD
11, 4949–4993, 2014

Fasham, M. J. R., Flynn, K. J., Pondaven, P., Anderson, T. R., and Boyd, P. W.: Development of a robust ecosystem model to predict the role for iron in biogeochemical cycles: a comparison of results for iron-replete and iron-limited areas, and the SOIREE iron-enrichment experiment, Deep-Sea Res., 53, 333–366, 2006.

Gelbard, F., Tambour, Y., and Seinfeld, J. H.: Sectional representations for simulating aerosol dynamics, J. Colloid Interf. Sci., 76, 541–556, 1980.

Gervais, F., Riebesell, U., and Gorbunov, M. Y.: Changes in primary productivity and chlorophyll *a* in response to iron fertilization in the southern Polar Frontal Zone, Limnol. Oceanogr., 47, 1324–1335, 2002.

Guidi, L., Jackson, G., A., Stemmann, L., Miquet, J. C., Picheral, M., and Gorsky, G.: Relationship between particle size distribution and flux in the mesopelagic zone, Deep-Sea Res. Pt. I, 55, 1364–1374, doi:10.1016/j.dsr.2008.05.014, 2008.

Hoffmann, L. J., Peeken, I., Lochte, K., Assmy, P., and Veldhuis, M.: Different reactions of Southern Ocean phytoplankton size classes to iron fertilization, Limnol. Oceanogr., 51, 1217–1229, 2006.

Jackson, G. A.: Comparing observed changes in particle size spectra with those predicted using coagulation theory, Deep-Sea Res. Pt. II, 42, 159–184, 1995.

Jackson, G. A.: Coagulation theory and models of oceanic plankton, in: Flocculation in Natural and Engineered Environmental Systems, edited by: Droppo, I., Leppard, G., Liss, S., and Milligan, T., CRC Press, Boca Raton, FL, 271–292, 2005.

Jackson, G. A. and Kiørboe, T.: Maximum phytoplankton concentrations in the sea, Limnol. Oceanogr., 53, 395–399, 2008.

Jackson, G. A. and Lochmann, S. E.: Effect of coagulation on nutrient and light limitation of an algal bloom, Limnol. Oceanogr., 37, 77–89, 1992.

Jackson, G. A., Waite, A. M., and Boyd, P. W.: Role of algal aggregation in vertical carbon export during SOIREE and in other low biomass environments, Geophys. Res. Lett., 32, L13607, doi:10.1029/2005GL023180, 2005.

Jassby, A. and Platt, T.: Mathematical formulation of the relationship between photosynthesis and light for phytoplankton, Limnol. Oceanogr., 21, 540–547, 1976.

Jouandet, M. P., Blain, S., Metzl, N., Brunet, C., Trull, T. W., and Obernosterer, I.: A seasonal carbon budget for a naturally iron-fertilized bloom over the Kerguelen Plateau in the Southern Ocean, Deep-Sea Res. Pt. II, 55, 856–867, doi:10.1016/j.dsr2.2007.12.037, 2008.

BGD
11, 4949–4993, 2014

Jouandet, M. P., Trull, T. W., Guidi, L., Picheral, M., Ebersbach; F., Stemmann, L., and Blain, S.: Optical imaging of mesopelagic particles indicates deep carbon flux beneath a natural iron-fertilized bloom in the Southern Ocean, Limnol. Oceanogr., 5, 1130–1140, 2011.

Lasbleiz, M., Leblanc, K., Claustre, H., Uitz, J., Cornet-Barthaux, V., Ouhssain, M., Ras, J., and Quéguiner, B.: Particulate matter distribution in relation to phytoplankton community structure in the Fe-fertilized Kerguelen region of the Southern Ocean during autral spring (KEOPS2), 2014.

Lampitt, R. S., Wishner, K. F., Turley, C. M., and Angel, M. V.: Marine snow studies in the Northeast Atlantic Ocean: distribution, composition and role as a food source for migrating plankton, Marine Biol., 116, 689–702, 1993.

Laurenceau et al.: The relative importance of phytodetrital aggregates and fecal pellets in the control of export fluxes from naturally iron-fertilised waters near the Kerguelen plateau, 2014.

Martin, P., Rutgers van der Loeff, M., Cassar, N., Vandromme, P., d'Ovidio, F., Stemmann, L., Rengarajan, R., Soares, M., González, H. E., Ebersbach, F., Lampitt, R. S., Sanders, R., Barnett, B. A., Smetacek, V., and Naqvi, S. W. A.: Iron fertilization enhanced net community production but not downward particle flux during the Southern Ocean iron fertilization experiment LOHAFEX, Global Biogeochem. Cy., 27, 1–11, doi:10.1002/gbc.20077, 2013.

Moore, J. K. and Abbott, M. R.: Surface chlorophyll concentrations in relation to the Antarctic Polar Front: seasonal and spatial patterns from satellite observations, J. Marine Syst., 37, 69–86, 2002.

Park, Y. H., Fuda, J. L., Durand, I., and Naveira Garabato, A.C: Internal tides and vertical mixing over the Kerguelen Plateau, Deep-Sea Res. Pt. II, 55, 583–593, 2008a.

Park, Y., Roquet, F., Fuda, J. L., and Durand, I.: Large scale circulation over and around the Kerguelen Plateau, Deep-Sea Res. II, 55, 566–581, doi:10.1016/j.dsr2.2007.12.030, 2008b.

Picheral, M., Guidi, L., Stemmann, L., Karl, D. M., Iddaoud, G., and Gorsky G: The Underwater Vision Profiler 5: An advanced instrument for high spatial resolution studies of particle size spectra and zooplankton, Limnol. Oceanogr.-Meth., 8, 462–473, doi:10.4319/lom.2010.8.462, 2010.

Planchon et al.: Carbon export in the naturally iron-fertilized Kerguelen area of the Southern Ocean using ^{234}Th-based approach, 2014.

Pollard, R. T., Venables, H. J., Read, J. F., and Allen, J. T.: Large scale circulation around the Crozet Plateau controls an annual phytoplankton bloom in the Crozet Basin, Deep-Sea Res. Pt. II, 54, 1905–1914, doi:10.1016/j.dsr2.2007.06.012, 2007.

BGD
11, 4949–4993, 2014

Pollard, R. T. et al.: Southern Ocean deep-water carbon export enhanced by natural iron fertilization, Nature, 457, 577–580, doi:10.1038/nature07716, 2009.
Salter, I., Lampitt, R. S., Sanders, S., Poulton, A. J., Kemp, A. E. S., Boorman, B., Saw, K., and Pearce, R.: Estimating carbon, silica and diatom export from a naturally fertilized phytoplankton bloom in the Southern Ocean using PELAGRA: a novel drifting sediment trap, Deep-Sea Res. Pt. II, 2233–2259, doi:10.1016/j.dsr2.2007.07.008, 2007.
Savoye, N., Trull, T. W., Jacquet, S., Navez, J., and Dehairs, F.: ^{234}Th based export fluxes during a natural iron fertilization experiment in the southern ocean (KEOPS), Deep-Sea Res. Pt. II, 55, 841–855, doi:10.1016/j.dsr2.2007.12.036, 2008.
Small, L. F., Fowler, S. W., and Ümlü, M. U.: Sinking rates of natural copepod fecal pellets, Mar. Biol., 51, 233–241, 1979.
Smetacek, V. et al.: Deep carbon export from a Southern Ocean iron-fertilized diatom bloom, Nature, 287, 313–319, 2012.
Sommer, U.: Maximal growth rates of Antarctic phytoplankton: only weak dependence on cell size, Limnol. Oceanogr., 34, 1109–1112, 1989.
Stemmann, L., Picheral, M., and Gorsky, G.: Diel variation in the vertical distribution of particulate matter (> 0.15 mm) in the NW Mediterranean Sea investigated with the Underwater Video Profiler, Deep-Sea Res. Pt. I, 47, 505–31, 2000.
Timmermans, K. R., van der Wagt, B., and de Baar, H. J. W.: Growth rates, half-saturation constants, and silicate, nitrate, and phosphate depletion in relation to iron availability of four large, open-ocean diatoms from the Southern Ocean, Limnol. Oceanogr., 49, 2141–2151, 2004.
Tréguer, P. and LeCorre, P.: Manuel d'analyse des sels nutritifs dans l'eau de mer (Utilisation de l'autoAnalyseur II), 2nd edn., Laboratoire d'Océanographie chimique, Univ. de Bretagne Occidentale, 1975.
Turner, J. T.: Zooplankton fecal pellets, marine snow and sinking phytoplankton blooms, Aquat. Microb. Ecol., 27, 57–102, 2002.
Tyrrell, T., Merico, A., Waniek, J. J., Wong, C. S., Metzl, N., and Whitney, F.: Effect of seafloor depth on phytoplankton blooms in high-nitrate, low-chlorophyll (HNLC) regions, J. Geophys. Res., 110, 1–12, 2005.
Uitz, J., Claustre, H., Morel, A., and Hooker, S. B.: Vertical distribution of phytoplankton communities in open ocean: an assessment based on surface chlorophyll, J. Geophys. Res.-Oceans, 111, 1–23, doi:10.1029/2005JC003207, 2006.

BGD
11, 4949–4993, 2014

Venables, H. J., Pollard, R. T., and Popova, E. K.: Physical conditions controlling the development of a regular phytoplankton bloom north of the Crozet Plateau, Southern Ocean, Deep-Sea Res. Pt. II, 54, 1949–1965, doi:10.1016/j.dsr2.2007.06.014, 2007.
Waite, A. and Nodder, S. D.: The effect of in situ iron addition on the sinking rates and export flux of Southern Ocean diatoms, Deep-Sea Res. Pt. II, 48, 2635–2654, 2001.
Wassmann, P.: Retention vs. export food chains: processes controlling sinking loss from marine pelagic systems. Hydrobiologia, 363, 29–57, 1998.

BGD
11, 4949–4993, 2014

Table 1. Date and time of the casts performed at Station A3.

Station	Date (dd mm yyyy)	Time (hh.mm)	Mixed Layer depth (m)
A3-1	21 Oct 2011	2.20 a.m.	165
A3-2/1	15 Nov 2011	11.20 p.m.	143
A3-2/2	16 Nov 2011	7.50 a.m.	171
A3-2/3	16 Nov 2011	11.30 a.m.	138
A3-2/4	16 Nov 2011	7.15 p.m.	147
A3-2/5	17 Nov 2011	1.10 a.m.	123
A3-2/6	17 Nov 2011	5.30 a.m.	163
A3-2/7	17 Nov 2011	2.30 p.m.	124

BGD
11, 4949–4993, 2014

Table 2. Symbols and parameter values used for the model. Conversion constants include: Carbon to chlorophyll = 50 g C : g Chl *a*; carbon to nitrogen = 106 mol C : 16 mol N.

Symbol	Quantity	Value	Units	Reference
d_c	Conserved diameter		cm	
d_a	Apparent diameter		cm	
d_1	Median algal diameter	20	µm	
D_{fr}	Fractal dimension	2	–	
G	Specific growth rate		d^{-1}	
G_{max}	Maximum specific growth rate	0.45	d^{-1}	Timmermans et al. (2004)
I	Irradiance		$ly\,d^{-1}$	
I_o	Surface irradiance		$ly\,d^{-1}$	Evans and Parslow (1985)
k	Total light attenuation = $k_w + k_r P$		m^{-1}	
k_r	Coefficient for light attenuation by plants	0.03	$m^2(mmol\ N)^{-1}$	Fasham et al. (1990)
k_w	Light attenuation of water	0.04	m^{-1}	Fasham et al. (1990)
K_d	Half saturation constant	1	$mmol\,N\,m^{-3}$	Fasham et al. (2006)
K_z	Eddy diffusivity	100	$m^2\,d^{-1}$	Park et al. (2008a)
m	Particle mass		g	
$n(d)$	Number spectrum for diameter d		cm^{-4}	
$n(m)$	Number spectrum for mass m		$cm^{-3}\,g^{-1}$	
N	Nitrate concentration		$mmol\,N\,m^{-3}$	
Q_i	Particle mass in ith section		g	
r	Phytoplankton mortality rate	0.04	d^{-1}	Assmy et al. (2007)
r_p	Relative light limitation		–	
r_n	Relative nitrate limitation		–	
v_i	Settling velocity for particle in ith section		md^{-1}	
V	Particle volume			
α_I	Slope of photosyn. curve		$0.04\,ly^{-1}$	Evans and Parslow (1985)
α	Stickiness	1	–	Jackson et al. (2005)
β	Coagulation kernels			
${}^1\beta_{i,j,l}$, ${}^2\beta_{i,l}$, ${}^3\beta_{l,l}$, ${}^4\beta_{i,l}$	Sectional coefficients			
ϕ	Phytoplankton concentration		$mmol\,N\,m^{-3}$	
λ_i	Disaggregation coef. for ith section		d^{-1}	Jackson (1995)
γ	Fluid shear	1	s^{-1}	Jackson et al. (2005)
μ	Average algal growth rate		d^{-1}	

BGD
11, 4949–4993, 2014

Table 3. Comparison of the POC fluxes (F_{POC} in mg m^{-2} d^{-1}) derived from particle size distributions from the UVP, particle distributions from gel-filled sediment traps and sediment trap PPS3/3 Technicap Inc, France (Laurenceau et al., 2014) during KEOPS2 and KEOPS1 (Jouandet et al., 2011; Ebersbach et al., 2008).

		Winter KEOPS2	Spring KEOPS2	Mid summer KEOPS 1	End summer KEOPS1
F_{POC} at 200 m (mg m^{-2} d^{-1})	$F = Ad^b$	1.75	23.11	869	58
	Gel trap		66		
	trap		27 ± 8		
F_{POC} at 350 m (mg m^{-2} d^{-1})	$F = Ad^b$	1.04	3.50	326	67

BGD
11, 4949–4993, 2014

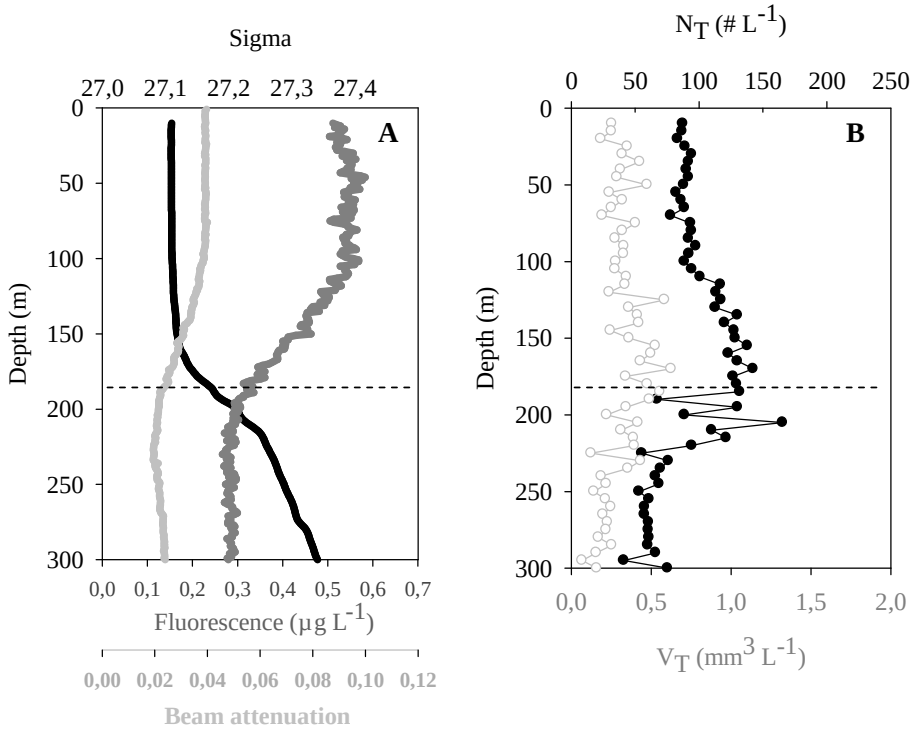

Fig. 1. Vertical distribution of sigma, fluorescence and turbidity **(A)** and vertical profiles of total abundance (N_T) and total volume (V_T) at the first cast of A3, during winter (A3-1, 21 October).

BGD
11, 4949–4993, 2014

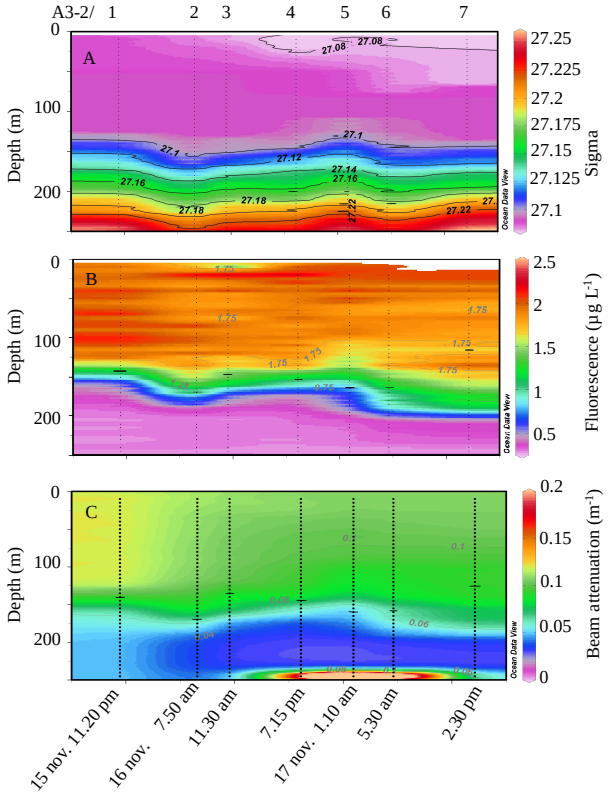

Fig. 2. Temporal evolution of density **(A)**, fluorescence **(B)** and turbidity **(C)** during the spring survey. The black lines show the mixed layer depth.

BGD
11, 4949–4993, 2014

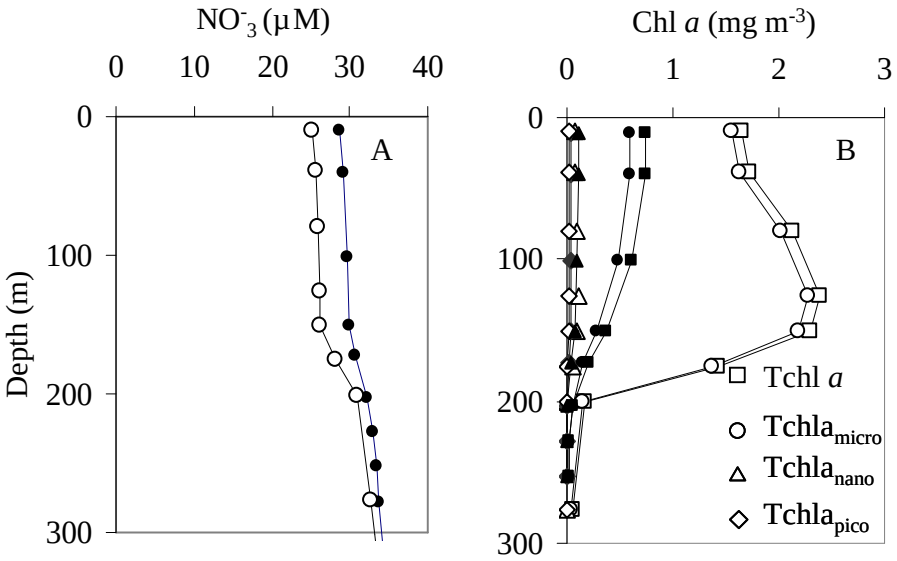

Fig. 3. Vertical distribution of the concentration of NO_3 **(A)**; Tchl *a*, and Tchl *a* associated with micro-(Tchl a_{micro}), nano-(Tchl a_{nano}), and picophytoplankton (Tchl a_{pico}) **(B)**.

BGD
11, 4949–4993, 2014

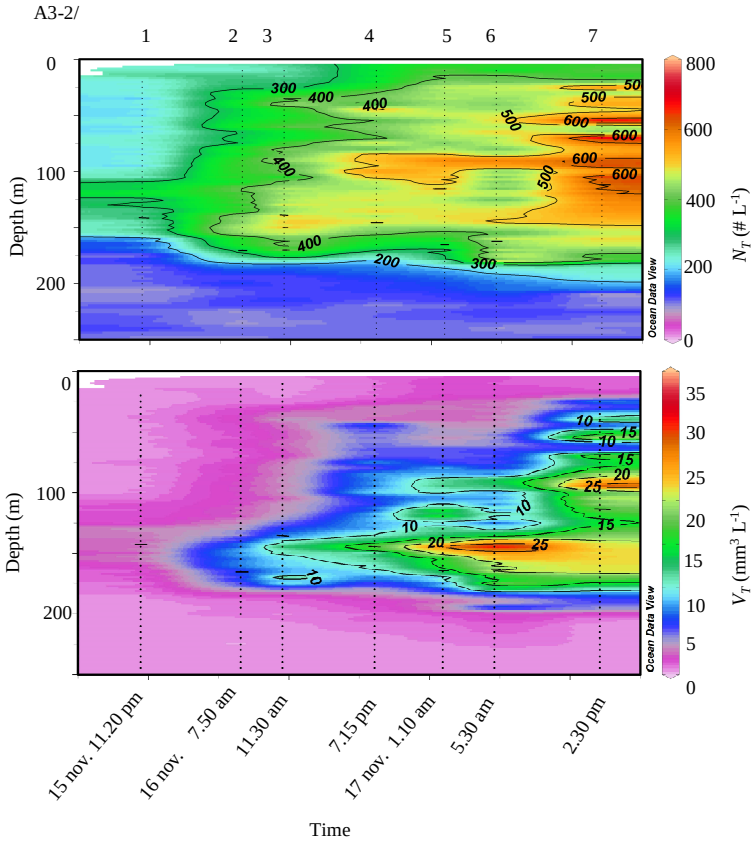

Fig. 4. Vertical distribution of N_T and V_T for the different casts during spring bloom.

BGD
11, 4949–4993, 2014

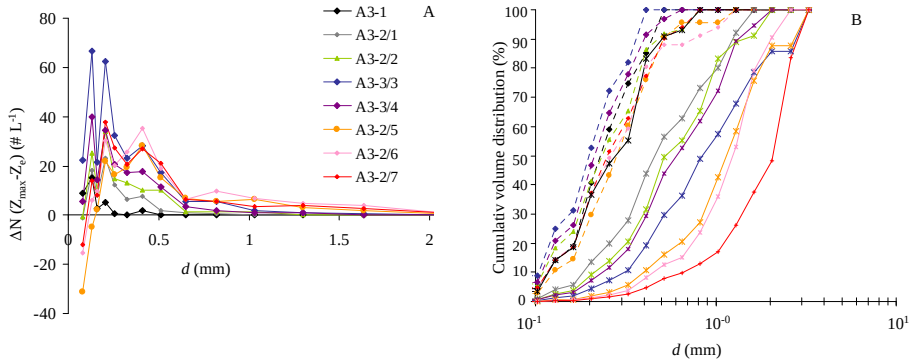

Fig. 5. Difference of the size spectra abundance between the depth of the volume maxima (Z_{max}) and the euphotic layer (Z_e) **(A)** and cumulative volume distribution **(B)** in the euphotic layer (dashed line) and at the depth of the V_T sub surface maxima (solid line).

BGD
11, 4949–4993, 2014

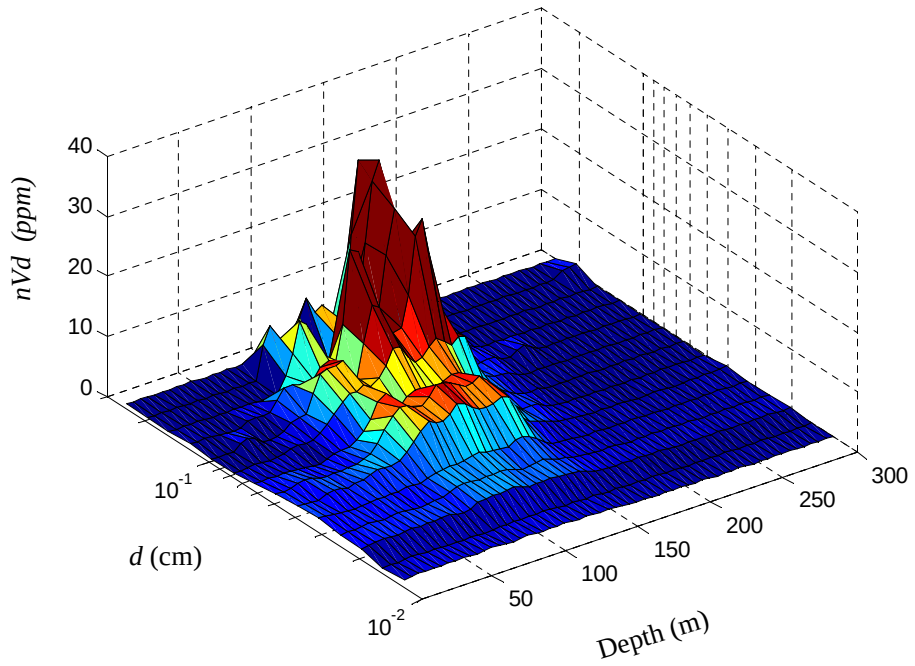

Fig. 6. Volume distribution size spectra along vertical axis on the 17 of November at 1.10 a.m. (A3-2/5).

BGD
11, 4949–4993, 2014

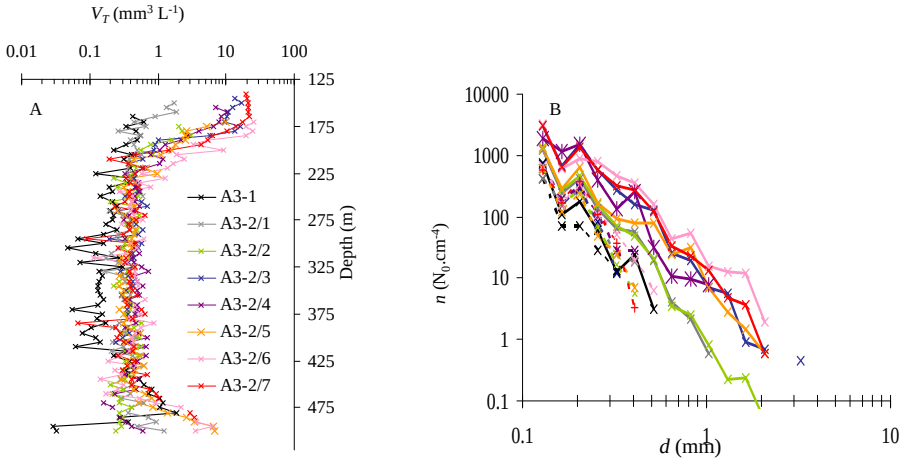

Fig. 7. Distribution of V_T below the surface mixed layer **(A)**. Normalized particles size spectra abundance average over the 320–350 layer (dotted line) and 100–200 m layer (solid line) **(B)**.

BGD
11, 4949–4993, 2014

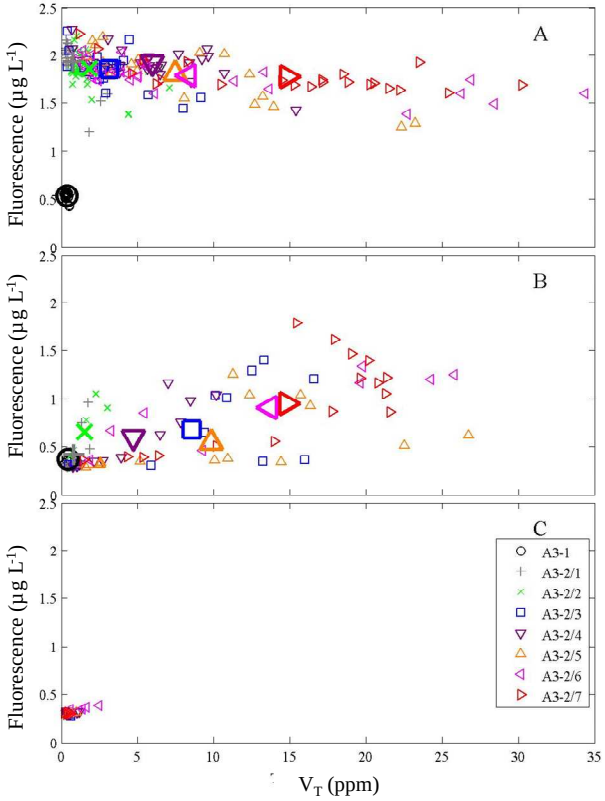

Fig. 8. Scatter plots of fluorescence and V_T for the 3 layers: surface to base of ML **(A)**, base of ML to 200 **(B)** and > 200 m **(C)**.

BGD
11, 4949–4993, 2014

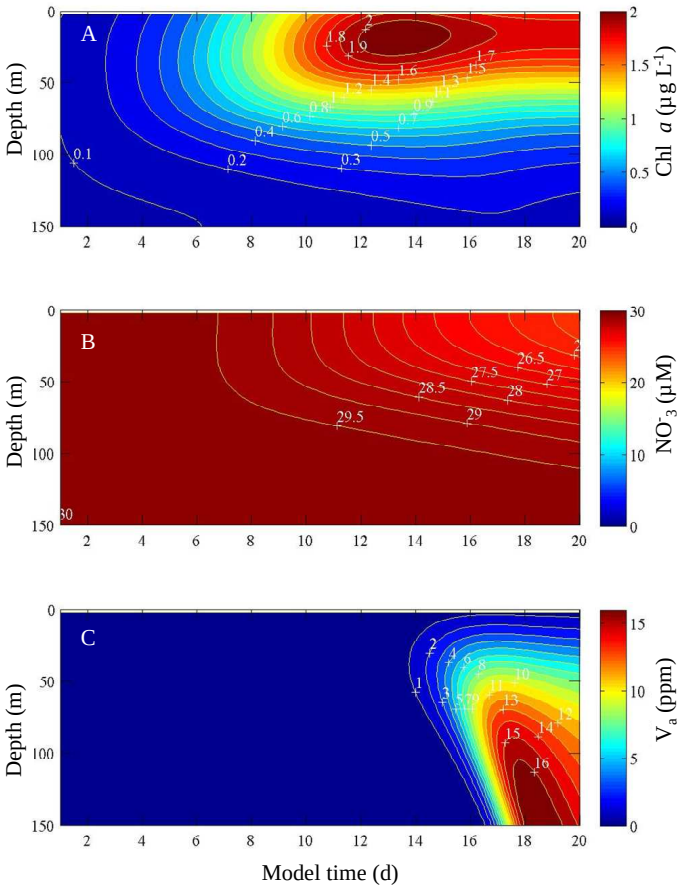

Fig. 9. Model results for vertical distribution through time of phytoplankton (µg Chl L^{-1}) (A; *phytoplankton concentration does not include any algae present in aggregates*), nitrate (µM) **(B)**, and V_{Ta} (ppm) **(C)**. Contour interval is 0.1 µg Chl L^{-1} **(A)**, 0.5 µM **(B)**, 1 ppm **(C)**. The calculation assumes that the UVP only measures aggregates larger than 100 µm.

BGD
11, 4949–4993, 2014

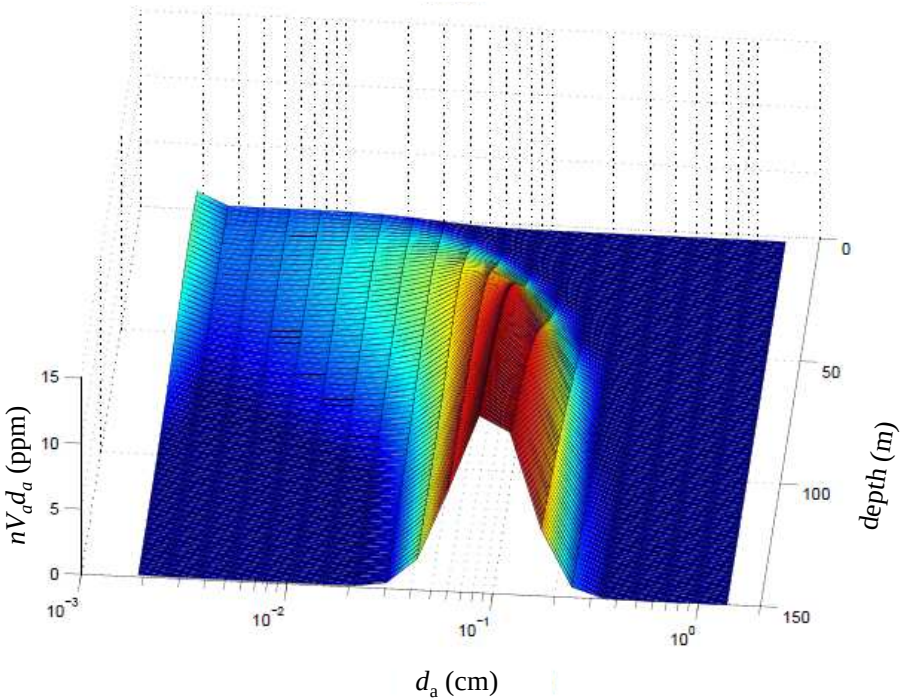

Fig. 10. Distribution of apparent particle volume, $nV\,d_a$, as a function of depth and d_a as calculated by the model at 20 d. Because the value of d_a is plotted on a logarithmic scale, the area under the curve for each depth is proportional to total particle volume V_{Ta}.

BGD
11, 4949–4993, 2014

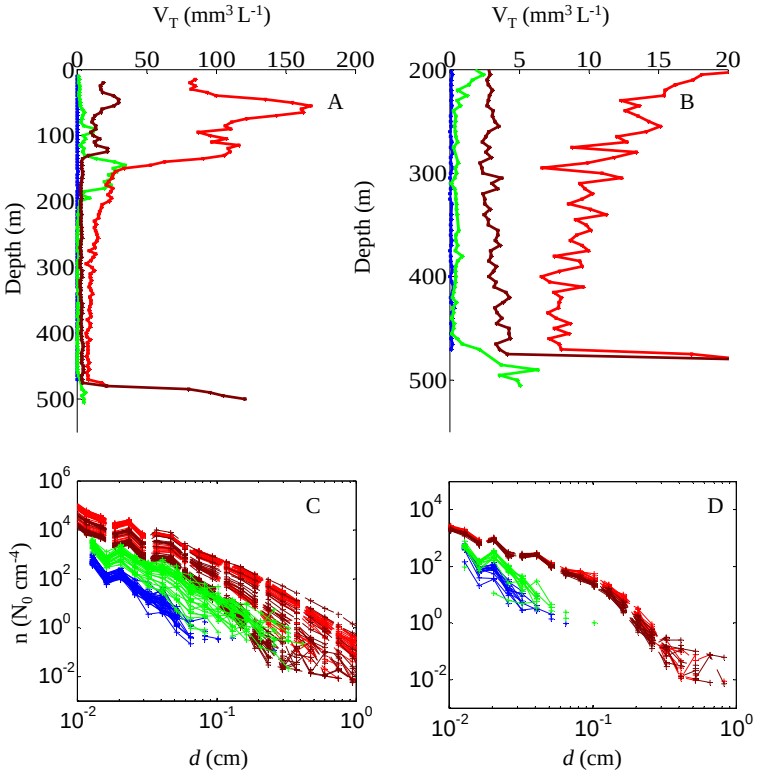

Fig. 11. (A) Comparison of the total volume profiles measured during KEOPS2 in October (A3-1, blue), November (A3-2/7, green), and during KEOPS1 in January (red) and February (brown). **(B)** Comparison of the normalised size spectra in the 0–200 m **(A)** and 200–400 m layer **(B)** in October (A3-1, blue), November (A3-2/7, green), and during KEOPS1 in January (red) and February (brown).

BGD
11, 4949–4993, 2014